Room-Temperature Sputtered Nanocrystalline Nickel Oxide as Hole Transport Layer for *p–i–n* Perovskite Solar Cells

*Erkan Aydin, Joel Troughton, Michele De Bastiani, Esma Ugur, Muhammad Sajjad, Areej Alzahrani, Marios Neophytou, Udo Schwingenschlögl, Frédéric Laquai, Derya Baran and Stefaan De Wolf**

King Abdullah University of Science and Technology (KAUST), KAUST Solar Center (KSC), Physical Sciences and Engineering Division (PSE), Thuwal 23955-6900, Kingdom of Saudi Arabia

Corresponding Author

*Stefaan De Wolf

stefaan.dewolf@kaust.edu.sa

Keywords: perovskites solar cells, room-temperature processing, sputtering, nickel oxide, conformal deposition, large area, p-i-n perovskite device configuration

Nickel oxide (NiO_x) is a promising hole transport layer (HTL) for perovskite solar cells (PSCs), as it combines good chemical stability, high broadband optical transparency and a high work function. Excellent power conversion efficiencies (PCE) have already been reported using solution-processed NiO_x. However, solution-based techniques usually require high-temperature post-annealing to achieve the required HTL properties of NiO_x, which jeopardizes its use for many applications, such as monolithic tandem solar cells. To resolve this issue, we developed room-temperature sputtered NiO_x and demonstrated *p–i–n* PSCs with 17.6% PCE (with negligible hysteresis), which is comparable to the best PSCs using sputtered and annealed NiO_x without heteroatom doping. Through detailed characterization and density functional theory (DFT) analysis, we explored the electrical and optical properties of the obtained NiO_x films and find that they are strongly linked with the specific defect chemistry of this material. Finally, in view of its use in perovskite/silicon tandem solar cells, we find that direct sputtering on random-pyramid textured silicon wafers results in highly conformal NiO_x films.

In the past eight years, the PCE of perovskite solar cells (PSCs) has quickly risen. Thanks to their excellent electronic and optical properties such as a high absorption coefficient[1] with sharp absorption onset,[2] photocurrents for thin-film solar cells are now already close to the theoretical limit. In addition, a high charge-carrier mobility,[3] long charge-carrier diffusion length[4] as well as a low Urbach energy[5] enable a very low open-circuit voltage (V_{OC}) deficit, explaining further their remarkable recent rise as a prominent photovoltaic technology. PSCs can be fabricated either in *n–i–p* or *p–i–n* configurations, depending on the relative position of the charge transport layers.[6] Among these two device configurations, the *n–i–p* structure has recently reached record power conversion efficiencies (PCE) in excess of 23%;[7-8] such devices are usually built onto metal-oxide based electron transport layers (ETL, e.g. TiO_2, SnO_2, ZnO).[9-11] On the other hand, although *p–i–n* configuration devices provides ease of fabrication, the limited choice of solvent-compatible hole transport layers HTLs and the lack of efficient *p*-type metal oxides hampers the further development of *p–i–n* PSCs. In fact, such HTLs have been limited to polymer-based HTL materials for several years (e.g. PEDOT:PSS). Nevertheless, developing a high-performance HTL has significant importance for the fabrication of *p–i–n* configuration top cells in perovskite/silicon tandem solar cell applications. Replacing organic HTLs with inorganic alternatives is of utmost importance to improve processing and device robustness, and also offers increased versatility in choice of materials. To this end, CuI, Cu_2O, CuSCN, CuPc, and NiO_x have shown promise for PSCs.[12-16] Of these, >20% PCE for opaque devices has been recently realized for CuSCN and NiO_x.[14-15] Both materials offer promising characteristics such as high broadband transparency and a high work function (WF), resulting in a good energy-alignment with the perovskite, enabling high V_{OC}. Moreover, in contrast to CuSCN, NiO_x chemically withstands most of the solvents used in PSC fabrication. By now, NiO_x has already been studied

widely with several successful reports employing solution-processing techniques such as sol-gel, combustion methods, and vacuum-based depositions including sputtering, pulsed-laser deposition, and atomic layer deposition.[15, 17-19] Recently, PSCs based on thin nanoparticle films of NiO_x synthesized by combustion were reported with PCEs in excess of 20%.[15] However, most of these studies require a high-temperature annealing step to activate the HTL properties, which hinders its use on substrates with limited temperature resilience, such as polyethylene terephthalate (PET). Low-temperature processing compatibility is also crucial for monolithic perovskite/silicon tandem solar applications relying on bottom cells with limited temperature resilience,[20] such as silicon heterojunction (SHJ) solar cells[21] (which are only compatible with top-cell fabrication processes up to ≈200 °C).[22-23] Moreover, solution-based deposition techniques on a random-pyramid textured silicon solar cells tend to result in poor surface coverage since polymer HTLs accumulate within the valleys during annealing.[20] These limitations motivated us to explore RF sputtering deposition at room-temperature for conformal deposition on both flat and textured surfaces. To date, the PCE of planar PSCs utilizing RF-sputtered NiO_x is limited to 16.2%.[18] The limited conductivity, mobility, and optical transparency appear currently to be roadblocks in reaching efficiencies in excess of 20%. Therefore, a detailed understanding of the defect structure of NiO_x is crucial to improve its HTL properties. To this end, we elucidate in this article how the defect structure of NiO_x films correlates with the material's properties. Following HTL optimization, we obtained *p–i–n* methylammonium lead iodide ($MAPbI_3$) based PSCs with PCEs of 17.6%.

Regarding the properties of our NiO_x layers, figures 1.a and 1.b show the compact nature of device-optimized 25 nm NiO_x films on polished quartz substrates investigated by AFM surface topography and SEM surface image analysis, respectively. Figure S3 shows the conformal

deposition of NiO_x films also on random pyramids textured wafers which are promising for fully textured perovskite/silicon tandem solar cells. To confirm the degree of crystallinity and phase analysis of the films, we performed surface-sensitive grazing incidence X-ray diffraction (GIXRD) measurements since standard thin-film XRD showed no reflection in the scanned region. GIXRD measurements (Figure 1.d) revealed the cubic structure of NiO_x as evidenced by the peaks located at ≈37.2° and ≈43.2° (2θ), which represent the (111) and (200) planes, respectively (JCPDS PDF No: 47-1049).[24] The observation of these peaks is in line with earlier reports for NiO_x films deposited at low-temperature and under pure argon atmosphere.[24] XRD analysis of step-wise annealed NiO_x films (from 100 to 700 °C, 100 °C steps, on quartz substrates) demonstrated that sputtered NiO_x does not exhibit evolution of any significant peak, even after annealing at high temperatures (Figure S1), which confirms the limited effect of annealing on the crystallite size. The crystallite sizes (D) of the NiO_x films are calculated to be 9.9 nm for as-deposited NiO_x following the Scherrer formula,[25] which is consistent with an average crystallite size of 8-9 nm as determined by AFM analysis (Figure S2).

Figure 1.e confirms the high broadband transparency of our sputtered NiO_x; assuming direct optical transitions, i.e. n = 2 in the Tauc relation $(\alpha h\upsilon) = B\,(h\upsilon - Eg)^{1/n}$, the optical band gap is calculated to be 3.55 eV for optimized NiO_x films, which is very close to the previously reported results (Figure S4).[26-27] Notably, annealing of the NiO_x films at 500 °C results in a decrease in optical transparency (Figure S5), indicating an increasing presence of interstitial O atoms within the NiO_x lattice.[28,29] Increasing process temperature or post-annealing process usually results in decreased Ni/O concentration ratio in the resultant films.[30-31] This compositional change might be responsible for the decreased conductivity of the NiO_x films after post-annealing process (Table S2). We should note that, the concentration of the microstructural defects of the as

deposited films has a strong impact on the electrical conductivity of the post-annealed samples. Therefore, by controlling the defect chemistry of the as deposited films, post-annealing process can be eleminated.

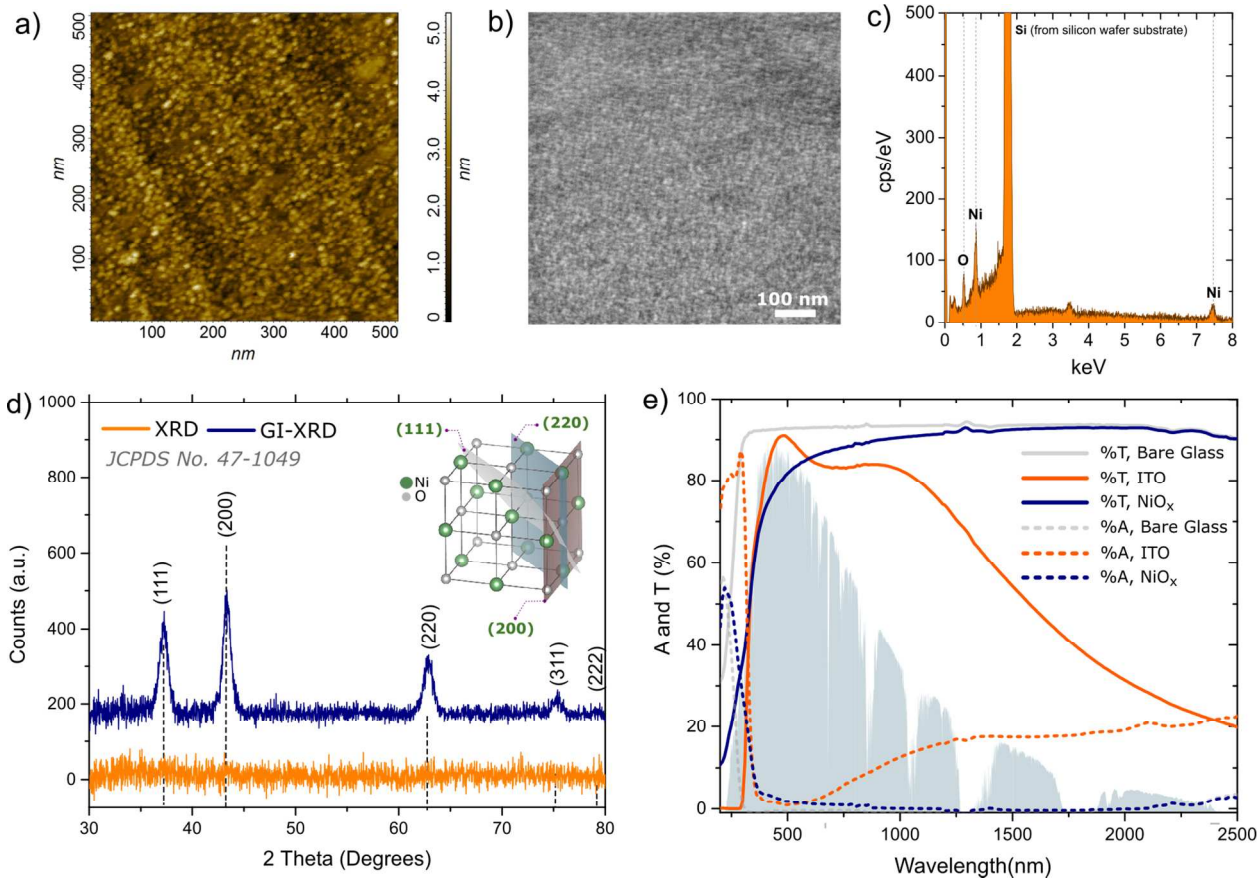

Figure 1. a) AFM surface topography, b) SEM surface image, c) EDX spectra, d) XRD analysis (The inset figure shows the prominent crystallographic planes of NiO_x), and e) transmittance (T), and absorptance (A) spectra of the sputtered NiO_x films measured with integrating sphere. The shaded gray area shows the spectral irradiance for AM 1.5 conditions. Absorptance was determined from 100-T-R.

The composition and defect density of the NiO_x films determines their optoelectronic properties and hence device performance. In this regard, elemental quantification energy-dispersive X-ray spectroscopy (EDX) analysis was performed on NiO_x films deposited on pre-etched silicon wafers to prevent any O contribution from the substrate. EDX analysis reveals on average 56% O and 44% Ni atomic ratios, suggesting O-rich nature of the films (Figure 1.c). The sputtering of

the NiO_x films was performed in a pure argon atmosphere to avoid further oxidation of the films. The dependency of the sputtering yield to the atomic mass of the target (atomic mass of oxygen (O) and nickel (Ni) is 15.99 and 58.69 u, respectively) may explain the observed Ni vacancy (V_{Ni}) and O interstitial (O_i) and therefore the existence of Ni^{3+} ions in the structure. X-ray photoelectron spectroscopy (XPS) spectra of the films are given in Figure 2.a, showing Ni $2p_{3/2}$ peaks in NiO_x. These spectra typically feature a main peak at ≈854 eV, shoulder at ≈856 eV, and shake-up satellite peak at ≈862 eV.[32-35] The peak centered at a binding energy of 853.7 and 855.6 eV can be ascribed to Ni^{2+} which is characteristic of the standard Ni–O octahedral bonding configuration of the cubic NiO_x rock salt and a vacancy induced Ni^{3+} ion, respectively.[36] The broad peak centered at 860.5 eV is attributed to shake-up.[37-38] The corresponding high-resolution O 1s scans are shown in Figure 2.b. The spectra show a narrow peak at a lower binding energy of 529.5 eV, which arises from octahedral bonding of Ni–O, and a broader component at 531.2 eV. This likely stems from defect sites within the NiO_x crystal lattice and may be ascribed to O interactions with a Ni-deficient lattice and nickel-hydroxides, including defective NiO with hydroxyl groups adsorbed onto the surface.[33-34, 39-40] The coexistence of Ni^{2+} and Ni^{3+} states is in line with the non-stoichiometric nature of the NiO_x film; their compositional ratio can be calculated by integrating the respective area for Ni^{3+} and Ni^{2+} on XPS spectra. The area ratio of 1.66 confirms the O-rich structure of the films. The Ni^{3+} in the structure forms a small portion of Ni_2O_3 within the film. As this phase is not distinguishable on the XRD graphs, we hypothesize it structurally to be amorphous.[41] Calculated DFT formation energies of Ni and O vacancies (1.18 eV and 4.40 eV, respectively) show that Ni vacancies are easier to form than O vacancies, agreeing with our experimental results that NiO is metal deficient. Hence, the *p*-type character of NiO is governed by the Ni vacancies, acting as acceptors. After formation of a Ni vacancy, the

structure relaxes and the nearest O/Ni atoms around the Ni vacancy move outwards/inwards (see Figure 2.d) as observed previously.[42] According to the density of states (DOS) shown in Figure 2.e, Ni vacancies in bulk NiO result in energy levels near the top of the valence band (shallow acceptor levels). These states enhance the *p*-type character (hole concentration). We suggest that this process results in increased hole conductivity.

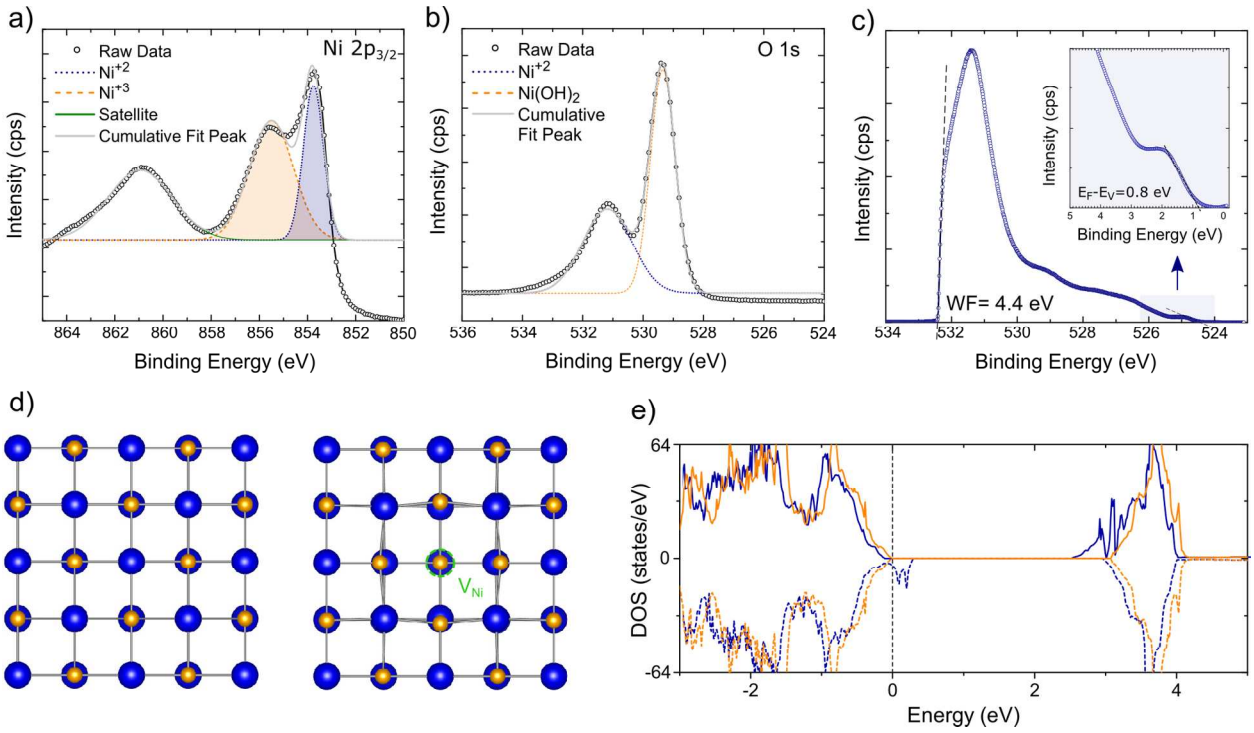

Figure 2. XPS survey spectra of a) Ni $2p_{3/2}$ and b) O1s states for sputtered NiO_x films. c) UPS spectra of NiO_x films. The inset figure shows a detailed view of the valence band edge. d) Atomic models for pristine (NiO) and defective (NiO_x) crystals ($Ni_{31}O_{32}$ which corresponds to 3.2% (i.e. 1/31) Ni vacancy doping, or Ni:O = 31/32 = 0.97). e) Spin-up (solid lines) and spin-down (dashed lines) DOS of pristine (Ni:O = 32/32 orange lines) and defective (Ni:O = 31/32, blue lines) NiO. The energy zero is set to the valence band maximum or Fermi level.

Conduction in NiO_x films occurs via localized Ni^{3+} states.[43-44] Thus the carrier mobility is associated with the density of these localized states. The measured Hall mobility of the films is 0.52 $cm^2/(Vs)$, which is in the expected range for pure-Ar sputtered NiO_x films (Table S2).[45]

Such a relatively high hole mobility compared to other successful *p*-type materials underlines their promising HTL character (see the comparison in Table S3).

To evaluate the performance of solar cells featuring sputtered NiO_x films, we fabricated *p–i–n* PSCs in the structure of ITO/NiO_x/$MAPbI_3$/PCBM/BCP/Ag, using 6,6-Phenyl C_{61} butyric acid methyl ester (PCBM) and bathocuproine (BCP) back electrodes (see Figure 3.a). We optimized the properties of the NiO_x layer towards high device performance by engineering the sputtering parameters (Figure S8). The stacked layers of the optimized device were analyzed by cross-sectional SEM, resulting in layer thicknesses of ~120 nm, ~25 nm, ~350 nm, ~60 nm, and ~100 nm for ITO, NiO_x, $MAPbI_3$, PCBM, and Ag, respectively. The thickness of the BCP layer is <5nm and undetectable in SEM (see Figure 3.b). Top view SEM, XRD, and UV-vis-NIR measurements (Figure S6) were also carried out to probe the formation of smooth and homogenous $MAPbI_3$ crystal thin films on NiO_x layers. Figure S7.a (Figure S7.b) shows the SEM image of a typical pinhole-free and uniform perovskite film on glass (on NiO_x). The corresponding XRD spectra of the perovskite thin film (Figure S7.c) shows no obvious PbI_2 or other non-perovskite phases, further confirming the film quality.

Figure 3.d depicts the J–V curve of the champion device, which has a PCE of 17.60% with a short-circuit current density J_{SC} = 20.65 mA cm^{-2}, V_{OC} = 1.078 V and FF = 0.79, measured under AM1.5G conditions. The integrated photocurrent of 20 mA cm^{-2} from the EQE spectra matches well with the J–V results (Figure 3.c and 3.e). As shown in Figure 3.f, devices retain their initial efficiency over 10 minutes when held at their maximum power point in nitrogen atmosphere.

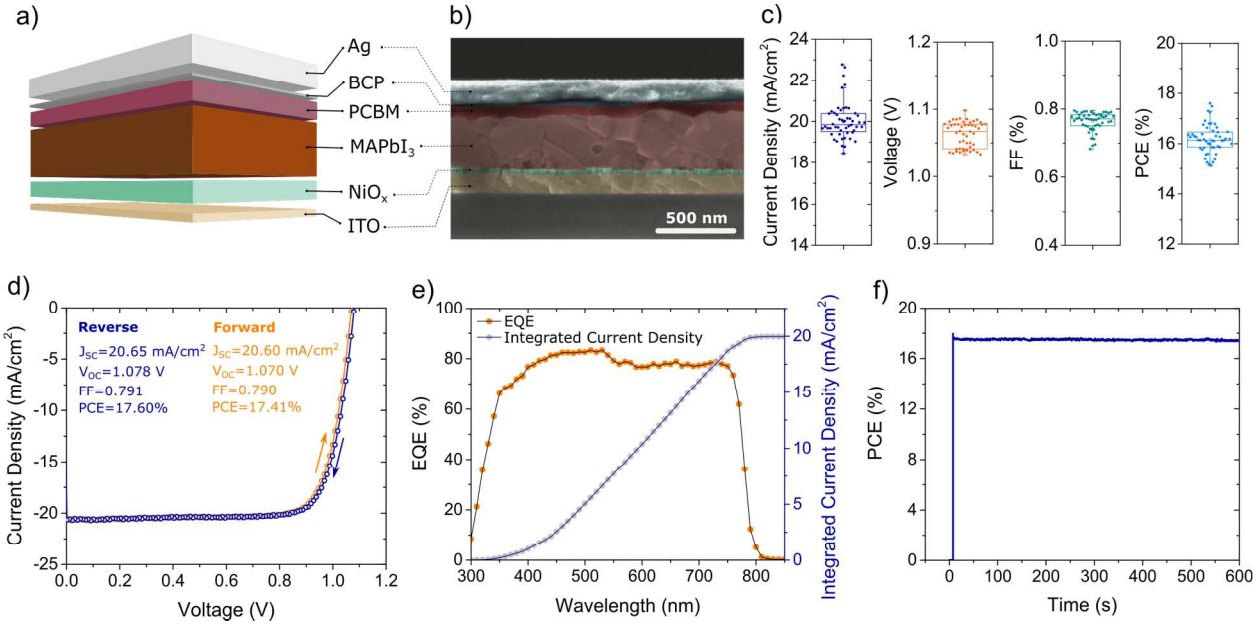

Figure 3. a) Schematic structure of the fabricated PSC with NiO_x as HTL. b) Cross-sectional SEM image of the device showing the individual layers. c) The statistical distribution of the device characteristics for 50 devices fabricated in different batches and associatively d) J–V characteristics of the champion device with optimized parameters. e) EQE spectra together with integrated current density. f) Stabilized efficiency of the champion device by J_{SC} tracking with time at a constant bias of 0.89 V with the controlled temperature at 25 °C. Note that all devices were tested at a 50 mV/s scan rate.

To investigate the carrier-recombination kinetics in $MAPbI_3$ in the presence of sputtered NiO_x layers, we performed time-resolved photoluminescence spectroscopy (TRPL). Figure 4.a shows 2D pseudo-color PL spectra of standalone $MAPbI_3$ films and $MAPbI_3/NiO_x$ junctions. As depicted in Figure 4.a, the perovskite thin films show the characteristic PL peak at 771 nm without any additional spectral feature. Carrier lifetimes following pulsed laser excitation at 650 nm were obtained by a single-exponential fit (Figure 4.b). From the fit of the PL decays, we find that the reference $MAPbI_3$ sample has PL lifetime of 135 ns, while the PL lifetime of the $MAPI_3/NiO_x$ junction is reduced to 92 ns. As the V_{OC} and photocurrent values of the sputtered-NiO_x based perovskite device are high, we may argue that the reduction in PL lifetime indicates efficient charge extraction and not increased non-radiative recombination.[46] [47-48] To further

investigate the charge-carrier transport dynamics and their effect on device performance, transient photocurrent (TPC) measurements were performed.

The dependency of the PCE and hysteresis response of the devices shown in Figure 4.c which reveals that NiO_x HTL based devices achieve the performance independently of the J–V scan speed over the range of 10 – 2000 mV/s. Transient photocurrent (TPC) measurements that use a step function for the optical excitation provided insight on carrier trapping and the effect of traps on carrier transport. Between the turn-on and turn-off dynamics, steady-state conditions were reached for over 100 μs. At early microsecond times, we observe non-monotonic turn-on dynamics with (recombination-active) increased light intensity, which might be correlated with traps at the electrode interface. However, the photocurrent reaches steady-state within 80 μs in all cases, and after turn-off of the light pulse decays within ~5 μs independent of the light intensity which demonstrates the limited influence of such trap states (Figure 4.d).

Ideally, HTLs should not induce an energetic barrier to the holes at the perovskite interface (due to a valence band offset, Δ_{VB}), whereas the conduction band offset (Δ_{CB}) should be sufficiently high to block electrons. To analyze these band offsets, the valence band maximum (V_{BM}) of the NiO_x films was determined by ultraviolet photoelectron spectroscopy (UPS). From the UPS cut-off spectra in Figure 2.c, we determine the work function of NiO_x to 4.4 eV, which is similar to literature-reported values.[18, 49] As shown in the inset of Figure 2.c, V_{BM} of the NiO_x is determined to be −5.20 eV, while the conduction band minimum (C_{BM}) is −1.65 eV when considering E_g = 3.55 eV. The energy-level diagram shows that $MAPbI_3$ (–5.43 eV) has a positive Δ_{VB} with sputtered NiO_x, equal to 0.23 eV (Figure 4.f). This is sufficiently small to achieve a low contact resistivity between NiO_x and $MAPbI_3$ without any significant effect on the

J–V curve.[50] Meanwhile, NiO_x provides efficient electron blocking properties owing to a sufficiently high Δ_{CB} at its interface with the V_{BM} of $MAPbI_3$ (−3.93 eV). We also calculated the band offsets by DFT using the electrostatic potential line-up method (Figure 4.e).[51] We obtain Δ_{VB} = 0.21 eV, which is consistent with the UPS results, and Δ_{CB} = 2.16 eV, confirming the electron-blocking properties of NiO_x. Figures 4.e and 4.f illustrate the DFT and experimental band offsets, respectively.

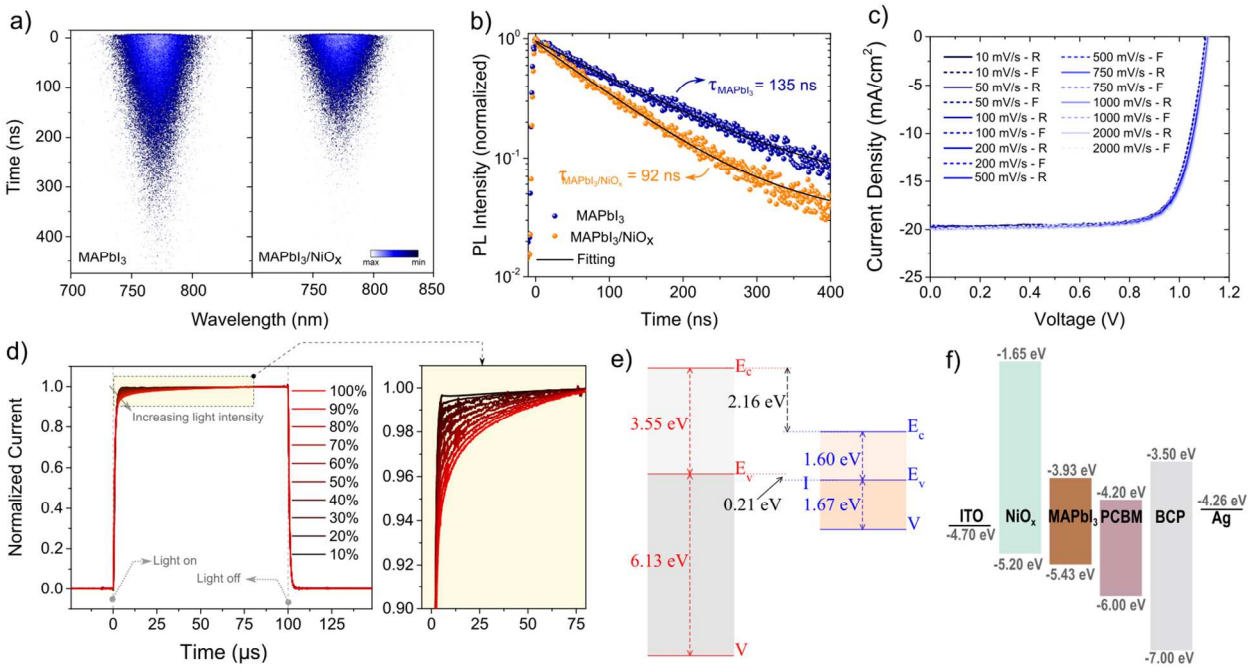

Figure 4. a) Streak camera images of $MAPbI_3$ and $MAPbI_3/NiO_x$ samples deposited on quartz substrates. The images show the evolution of the spectra with a time of the samples excited with 650 nm wavelength (fluence = 49 nJ/cm^2, laser frequency = 250 kHz). b) TRPL decay of the related samples probed at 771 nm. The initial carrier concentration after pulsed excitation was calculated as $n_0 = 8 \times 10^{15}$ cm^{-3}. c) J–V characteristics of the devices with different scan speeds varying from the ultra-slow and ultra-fast scan under standard AM1.5G solar illumination (100 mW cm^{-2}). d) Transient photocurrent behavior of the devices measured with a white LED at 100 µs square pulse together with a detailed view of rising and decaying periods. e) Valence and conduction band offsets (black numbers). V is the macroscopic average electrostatic potential of the bulk system. f) Energy levels of the stacked materials.

In summary, we provided a simple and effective fabrication recipe for all ≤100 °C processed *p–i–n* PSCs with 17.6% champion efficiency and negligible hysteresis, which is among the

highest reported for sputtered NiO_x without heteroatom doping, and irrespective of the applied thermal budget. In addition, we showed the potential application of room-temperature sputtered NiO_x films with perovskite/silicon tandem solar cells by depositing conformal layers on random pyramids textured wafers. We revealed that the electrical and optical properties of the optimized films are strongly connected to the defect chemistry of the NiO_x. For better HTL performances, the relatively low electrical conductivity and carrier concentration of the sputtered NiO_x can be increased by heteroatom doping. Previously, doping of sputtered NiO_x by cobalt and magnesium has been reported by elsewhere.[49, 52] Doping with other heteroatoms such as copper, zinc, silver may increase the hole transporting properties of NiO_x. We should note that although doping is beneficial for increased conductivity and mobility, optically it is usually accompanied with parasitic absorption losses potentially resulting in reduced photocurrents on the device level. Further progress of the PSC with sputtered NiO_x may be realized by contact passivation, and employing alternative ETLs that provide more suitable band alignment. Room-temperature processing of NiO_x opens a new avenue for the processing of organic and perovskites solar cells on readily available cost-efficient polymer foils and other temperature sensitive substrates. In conclusion, improved understanding of defect chemistry and the doping mechanism of the NiO_x offers new opportunities to improve the PCE with less parasitic absorption and enhanced charge extraction efficiency.

ASSOCIATED CONTENT

Supporting Information. Experimental parameters and DFT calculation details. XRD graphs of the annealed NiO_x thin films. Grain size and roughness analysis by AFM. SEM images of the NiO_x films on textured silicon wafers. $(\alpha h\nu)^2$ vs $h\nu$ graph of the NiO_x films. Comparison of

transmittance and absorbance spectra of the as-deposited and annealed NiO_x films. Transmittance, absorbance and reflectance spectra of the $MAPbI_3$ films. SEM surface morphology and XRD analysis of the $MAPbI_3$ films. The solar cell characteristics with different deposition conditions of NiO_x. Planar and macroscopic average electrostatic potentials. The table comparing the PCE of the devices with literature.

AUTHOR INFORMATION

Corresponding Author

*E-mail: stefaan.dewolf@kaust.edu.sa . Phone: +966 12 808 4849

ORCID

Erkan Aydin: 0000-0002-8849-2788

Joel Troughton: 0000-0003-2434-5655

Michele De Bastiani: XXXX-XXXX-XXXX-XXXX

Esma Ugur: 0000-0003-0070-334X

Muhammad Sajjad: 0000-0001-6659-9771

Areej Alzahrani: 0000-0002-5395-2975

Marios Neopthyou: XXXX-XXXX-XXXX-XXXX

Udo Schwingenschlögl: 0000-0003-4179-7231

Frédéric Laquai: 0000-0002-5887-6158

Derya Baran: 0000-0003-2196-8187

Stefaan De Wolf: XXXX-XXXX-XXXX-XXXX

Notes

The authors declare no competing financial interest.

ACKNOWLEDGMENT

The research reported in this publication was supported by funding from King Abdullah University of Science and Technology (KAUST).

REFERENCES

(1) Park, N.-G., Perovskite Solar Cells: an Emerging Photovoltaic Technology. *Mater. Today* **2015,** *18*, 65-72.

(2) De Wolf, S.; Holovsky, J.; Moon, S. J.; Loper, P.; Niesen, B.; Ledinsky, M.; Haug, F. J.; Yum, J. H.; Ballif, C. Organometallic Halide Perovskites: Sharp Optical Absorption Edge and its Relation to Photovoltaic Performance. *J. Phys. Chem. Lett.* **2014,** *5*, 1035-9.

(3) Wehrenfennig, C.; Eperon, G. E.; Johnston, M. B.; J. Snaith, H.; M. Herz, L. High Charge Carrier Mobilities and Lifetimes in Organolead Trihalide Perovskites. *Adv. Mater.* **2014,** *26*, 1584-1589.

(4) Stranks, S. D.; Eperon, G. E.; Grancini, G.; Menelaou, C.; Alcocer, M. J. P.; Leijtens, T.; Herz, L. M.; Petrozza, A.; Snaith, H. J. Electron-Hole Diffusion Lengths Exceeding 1 Micrometer in an Organometal Trihalide Perovskite Absorber. *Science* **2013,** *342*, 341-344.

(5) Sutter-Fella, C. M.; Miller, D. W.; Ngo, Q. P.; Roe, E. T.; Toma, F. M.; Sharp, I. D.; Lonergan, M. C.; Javey, A. Band Tailing and Deep Defect States in $CH_3NH_3Pb(I_{1-x}Br_x)_3$ Perovskites as Revealed by Sub-Bandgap Photocurrent. *ACS Energy Lett.* **2017,** *2*, 709-715.

(6) Giorgi, G.; Fujisawa, J.-I.; Segawa, H.; Yamashita, K. Small Photocarrier Effective Masses Featuring Ambipolar Transport in Methylammonium Lead Iodide Perovskite: A Density Functional Analysis. *J. Phys. Chem. Lett.* **2013,** *4*, 4213-4216.

(7) NREL Best Research-Cell Efficiencies. https://www.nrel.gov/pv/assets/images/efficiency-chart.png (accessed 26-07-18).

(8) Jeon, N. J.; Na, H.; Jung, E. H.; Yang, T.-Y.; Lee, Y. G.; Kim, G.; Shin, H.-W.; Il Seok, S.; Lee, J.; Seo, J. A Fluorene-Terminated Hole-Transporting Material for Highly Efficient And Stable Perovskite Solar Cells. *Nat. Energy* **2018**, 3, 682.

(9) Yang, W. S.; Park, B.-W.; Jung, E. H.; Jeon, N. J.; Kim, Y. C.; Lee, D. U.; Shin, S. S.; Seo, J.; Kim, E. K.; Noh, J. H.; Seok, S. I., Iodide Management in Formamidinium-Lead-Halide–Based Perovskite Layers for Efficient Solar Cells. *Science* **2017,** *356*, 1376-1379.

(10) Jiang, Q.; Zhang, L.; Wang, H.; Yang, X.; Meng, J.; Liu, H.; Yin, Z.; Wu, J.; Zhang, X.; You, J., Enhanced Electron Extraction using SnO_2 for High-Efficiency Planar-Structure $HC(NH_2)_2PbI_3$-based Perovskite Solar Cells. *Nat. Energy* **2016**, 2, 16177.

(11) Ugur, E.; Sheikh, A. D.; Munir, R.; Khan, J. I.; Barrit, D.; Amassian, A.; Laquai, F., Improved Morphology and Efficiency of *n–i–p* Planar Perovskite Solar Cells by Processing with Glycol Ether Additives. *ACS Energy Lett.* **2017,** *2*, 1960-1968.

(12) Han, J.; Tu, Y.; Liu, Z.; Liu, X.; Ye, H.; Tang, Z.; Shi, T.; Liao, G., Efficient and Stable Inverted Planar Perovskite Solar Cells using Dopant-Free CuPc as Hole Transport Layer. *Electrochim. Acta* **2018,** *273*, 273-281.

(13) Sun, W.; Ye, S.; Rao, H.; Li, Y.; Liu, Z.; Xiao, L.; Chen, Z.; Bian, Z.; Huang, C., Room-Temperature and Solution-Processed Copper Iodide as the Hole Transport Layer for Inverted Planar Perovskite Solar Cells. *Nanoscale* **2016,** *8*, 15954-15960.

(14) Arora, N.; Dar, M. I.; Hinderhofer, A.; Pellet, N.; Schreiber, F.; Zakeeruddin, S. M.; Grätzel, M., Perovskite Solar Cells with CuSCN Hole Extraction Layers Yield Stabilized Efficiencies Greater Than 20%. *Science* **2017**.

(15) Liu, Z.; Chang, J.; Lin, Z.; Zhou, L.; Yang, Z.; Chen, D.; Zhang, C.; Liu, S.; Hao, Y., High-Performance Planar Perovskite Solar Cells Using Low Temperature, Solution–Combustion-based Nickel Oxide Hole Transporting Layer with Efficiency Exceeding 20%. *Adv. Energy Mater.* **2018,** *0*, 1703432.

(16) Chuantian, Z.; Liming, D., Solution-Processed Cu_2O and CuO as Hole Transport Materials for Efficient Perovskite Solar Cells. *Small* **2015,** *11*, 5528-5532.

(17) Hoon, P. J.; Jangwon, S.; Sangman, P.; Sik, S. S.; Chan, K. Y.; Joong, J. N.; Hee-Won, S.; Kyu, A. T.; Hong, N. J.; Cheol, Y. S.; Seong, H. C.; Il, S. S., Efficient $CH_3NH_3PbI_3$ Perovskite Solar Cells Employing Nanostructured p-Type NiO Electrode Formed by a Pulsed Laser Deposition. *Adv. Mater.* **2015,** *27*, 4013-4019.

(18) Yan, X.; Zheng, J.; Zheng, L.; Lin, G.; Lin, H.; Chen, G.; Binbin, D.; Zhang, F., Optimization of Sputtering NiO_x Films for Perovskite Solar Cell Applications. *Mater. Res. Bull.* **2018**, 103, 150-157.

(19) Seo, S.; Park, I. J.; Kim, M.; Lee, S.; Bae, C.; Jung, H. S.; Park, N.-G.; Kim, J. Y.; Shin, H., An Ultra-Thin, un-Doped NiO Hole Transporting Layer of Highly Efficient (16.4%) Organic-Inorganic Hybrid Perovskite Solar Cells. *Nanoscale* **2016,** *8*, 11403-11412.

(20) Sahli, F.; Werner, J.; Kamino, B. A.; Bräuninger, M.; Monnard, R.; Paviet-Salomon, B.; Barraud, L.; Ding, L.; Diaz Leon, J. J.; Sacchetto, D.; Cattaneo, G.; Despeisse, M.; Boccard, M.; Nicolay, S.; Jeangros, Q.; Niesen, B.; Ballif, C., Fully Textured Monolithic

Perovskite/Silicon Tandem Solar Cells with 25.2% Power Conversion Efficiency. *Nat. Mater.* **2018**, 17, 820-826.

(21) De Wolf, S.; Descoeudres, A.; Holman, Z. C.; Ballif, C., High-efficiency Silicon Heterojunction Solar Cells: A Review. *Green* **2012,** *2*, 7-24.

(22) Battaglia, C.; Cuevas, A.; De Wolf, S., High-Efficiency Crystalline Silicon Solar Cells: Status and Perspectives. *Energy Environ. Sci.* **2016,** *9*, 1552-1576.

(23) Bush, K. A.; Palmstrom, A. F.; Yu, Z. J.; Boccard, M.; Cheacharoen, R.; Mailoa, J. P.; McMeekin, D. P.; Hoye, R. L. Z.; Bailie, C. D.; Leijtens, T.; Peters, I. M.; Minichetti, M. C.; Rolston, N.; Prasanna, R.; Sofia, S.; Harwood, D.; Ma, W.; Moghadam, F.; Snaith, H. J.; Buonassisi, T.; Holman, Z. C.; Bent, S. F.; McGehee, M. D., 23.6%-Efficient Monolithic Perovskite/Silicon Tandem Solar Cells with Improved Stability. *Nat. Energy* **2017**, 2, 17009.

(24) Chen, H.-L.; Yang, Y.-S., Effect 0f Crystallographic Orientations on Electrical Properties of Sputter-Deposited Nickel Oxide Thin Films. *Thin Solid Films* **2008,** *516*, 5590-5596.

(25) Sankir, N. D.; Aydin, E.; Unver, H.; Uluer, E.; Parlak, M., Preparation and Characterization of Cost Effective Spray Pyrolyzed Absorber Layer for Thin Film Solar Cells. *Sol. Energy* **2013,** *95*, 21-29.

(26) Lee, H.; Huang, Y.-T.; Horn, M. W.; Feng, S.-P., Engineered Optical and Electrical Performance of RF–Sputtered Undoped Nickel Oxide Thin Films for Inverted Perovskite Solar Cells. *Sci. Rep.* **2018,** *8*, 5590.

(27) Wang, K.-C.; Shen, P.-S.; Li, M.-H.; Chen, S.; Lin, M.-W.; Chen, P.; Guo, T.-F., Low-temperature Sputtered Nickel Oxide Compact Thin Film as Effective Electron Blocking

Layer for Mesoscopic $NiO/CH_3NH_3PbI_3$ Perovskite Heterojunction Solar Cells. *ACS Appl. Mater. Interfaces* **2014,** *6*, 11851–11858.

(28) Zhao, Y.; Wang, H.; Wu, C.; Shi, Z. F.; Gao, F. B.; Li, W. C.; Wu, G. G.; Zhang, B. L.; Du, G. T., Structures, Electrical and Optical Properties of Nickel Oxide Films by Radio Frequency Magnetron Sputtering. *Vacuum* **2014,** *103*, 14-16.

(29) Yang, J.-L.; Lai, Y.-S.; Chen, J. S., Effect of Heat Treatment on the Properties of Non-Stoichiometric *p*-Type Nickel Oxide Films Deposited by Reactive Sputtering. *Thin Solid Films* **2005,** *488*, 242-246.

(30) Kumar, S. C. a. M. C. S., Effect of Substrate Temperature and Oxygen Partial Pressure on RF Sputtered NiO Thin Films. *Mater. Res. Express* **2018**, 5, 046401.

(31) Lu, Y. M.; Hwang, W. S.; Yang, J. S., Effects of Substrate Temperature on The Resistivity of Non-stoichiometric Sputtered NiO_x Films. *Surf. Coat. Technol.* **2002,** *155*, 231-235.

(32) Wei, C.; Yinghui, W.; Jing, F.; B., D. A.; Fangzhou, L.; Won, T. H.; Annie, N.; Charles, S.; Kin, C. W.; Dong, W.; Zhu-Bing, H., Understanding the Doping Effect on NiO: Toward High-Performance Inverted Perovskite Solar Cells. *Adv. Energy Mater.* **2018,** *0*, 1703519.

(33) R., M. J.; Sai-Wing, T.; J., H. M.; Tzung-Han, L.; Song, C.; M., A. C.; R., R. J.; Franky, S., Solution-Processed Nickel Oxide Hole Transport Layers in High Efficiency Polymer Photovoltaic Cells. *Adv. Funct. Mater.* **2013,** *23*, 2993-3001.

(34) Sun, J.; Lu, J.; Li, B.; Jiang, L.; Chesman, A. S. R.; Scully, A. D.; Gengenbach, T. R.; Cheng, Y.-B.; Jasieniak, J. J., Inverted Perovskite Solar Cells with High Fill-factors

Featuring Chemical Bath Deposited Mesoporous NiO Hole Transporting Layers. *Nano Energy* **2018**, 49, 163-171.

(35) Nesbitt, H. W.; Legrand, D.; Bancroft, G. M., Interpretation of Ni2p XPS Spectra of Ni Conductors and Ni Insulators. *Phys. Chem. Miner.* **2000,** *27*, 357-366.

(36) You, J.; Meng, L.; Song, T.-B.; Guo, T.-F.; Yang, Y. M.; Chang, W.-H.; Hong, Z.; Chen, H.; Zhou, H.; Chen, Q.; Liu, Y.; Marco, N. D.; Yang, Y., Improved Air Stability of Perovskite Solar Cells via Solution-processed Metal Oxide Transport Layers. *Nat. Nanotechnol.* **2015,** *11*, 75-81.

(37) Kim, K. S.; Winograd, N., X-Ray Photoelectron Spectroscopic Studies of Nickel-Oxygen Surfaces using Oxygen and Argon Ion-Bombardment. *Surf. Sci.* **1974,** *43*, 625-643.

(38) Biesinger, M. C.; Payne, B. P.; Lau, L. W. M.; Gerson, A.; Smart, R. S. C., X-Ray Photoelectron Spectroscopic Chemical State Quantification of Mixed Nickel Metal, Oxide and Hydroxide Systems. *Surf. Interface Anal.* **2009,** *41*, 324-332.

(39) Langell, M. A.; Nassir, M. H., Stabilization of NiO(111) Thin Films by Surface Hydroxyls. *J. Phys. Chem.* **1995,** *99*, 4162-4169.

(40) Tomellini, M., X-Ray Photoelectron Spectra of Defective Nickel Oxide. *J. Chem. Soc., Faraday Trans. 1* **1988,** *84*, 3501-3510.

(41) Chen, W.-Y.; Jeng, J.-S.; Huang, K.-L.; Chen, J.-S., Modulation of Ni Valence in *p*-Type NiO Films via Substitution of Ni by Cu. *J.Vac. Sci. Technol. A* **2013,** *31*, 021501.

(42) Park, S.; Ahn, H.-S.; Lee, C.-K.; Kim, H.; Jin, H.; Lee, H.-S.; Seo, S.; Yu, J.; Han, S., Interaction and Ordering of Vacancy Defects in NiO. *Phys. Rev. B* **2008**, 77, 134103.

(43) Wei, Y.; Yao, K.; Wang, X.; Jiang, Y.; Liu, X.; Zhou, N.; Li, F., Improving the Efficiency and Environmental Stability of Inverted Planar Perovskite Solar Cells via Silver-Doped Nickel Oxide Hole-Transporting Layer. *Appl. Surf. Sci.* **2018,** *427*, 782-790.

(44) Chen, W.; Wu, Y.; Yue, Y.; Liu, J.; Zhang, W.; Yang, X.; Chen, H.; Bi, E.; Ashraful, I.; Grätzel, M.; Han, L., Efficient and Stable Large-Area Perovskite Solar Cells with Inorganic Charge Extraction Layers. *Science* **2015,** *350*, 944-948.

(45) Chen, H.-L.; Lu, Y.-M.; Hwang, W.-S., Characterization of Sputtered NiO Thin Films. *Surf. Coat. Technol.* **2005,** *198*, 138-142.

(46) Yang, Y.; Yang, M.; Moore, D. T.; Yan, Y.; Miller, E. M.; Zhu, K.; Beard, M. C., Top and Bottom Surfaces Limit Carrier Lifetime in Lead Iodide Perovskite Films. *Nat. Energy* **2017,** *2*.

(47) Stranks, S. D., Nonradiative Losses in Metal Halide Perovskites. *ACS Energy Lett.* **2017,** *2*, 1515-1525.

(48) Tress, W., Perovskite Solar Cells on the Way to Their Radiative Efficiency Limit – Insights Into a Success Story of High Open-Circuit Voltage and Low Recombination. *Adv. Energy Mater.* **2017,** *7*.

(49) Li, G.; Jiang, Y.; Deng, S.; Tam, A.; Xu, P.; Wong, M.; Kwok, H. S., Overcoming the Limitations of Sputtered Nickel Oxide for High-Efficiency and Large-Area Perovskite Solar Cells. *Adv. Sci.* **2017,** *4*, 1700463.

(50) Minemoto, T.; Murata, M., Theoretical Analysis on Effect of Band Offsets in Perovskite Solar Cells. *Sol. Energy Mater. Sol. Cells* **2015,** *133*, 8-14.

(51) Van de Walle, C. G.; Martin, R. M., Theoretical Study of Band Offsets at Semiconductor Interfaces. *Phys. Rev. B* **1987,** *35*, 8154-8165.

(52) Huang, A. B.; Zhu, J. T.; Zheng, J. Y.; Yu, Y.; Liu, Y.; Yang, S. W.; Bao, S. H.; Lei, L.; Jin, P., Achieving High-Performance Planar Perovskite Solar Cells with Co-sputtered Co-doping NiO_x Hole Transport Layers by Efficient Extraction and Enhanced Mobility. *J. Mater. Chem. C* **2016,** *4*, 10839-10846.

TOC GRAPHICS